Published in final edited form as:
Nano Lett. 2011 May 11; 11(5): 2096–2103. doi:10.1021/nl200636r.

Controlling *In Vivo* Stability and Biodistribution in Electrostatically Assembled Nanoparticles for Systemic Delivery

Zhiyong Poon, **Jong Bum Lee**, **Stephen W Morton**, and **Paula T Hammond**
The Koch Institute for Integrative Cancer Research at MIT, Department of Chemical Engineering, Massachusetts Institute of Technology, Cambridge, Massachusetts 02139, USA

Abstract

This paper demonstrates the generation of systemically deliverable layer-by-layer (LbL) nanoparticles for cancer applications. LbL-based nanoparticles designed to navigate the body and deliver therapeutics in a programmable fashion are promising new and alternative systems for drug delivery; but there have been very few demonstrations of their systemic delivery *in vivo* due to a lack of knowledge in building LbL nanofilms that mimic traditional nanoparticle design to optimize delivery. The key to the successful application of these nanocarriers *in vivo* requires a systematic analysis of the influence of film architecture and adsorbed polyelectrolyte outer layer on their pharmacokinetics, which has thus far not been examined for this new approach to nanoparticle delivery. Herein, we have taken the first steps in stabilizing and controlling the systemic distribution of multilayer nanoparticles. Our findings highlight the unique character of LbL systems: the electrostatically assembled nanoparticles gain increased stability *in vivo* with larger numbers of deposited layers, and the final layer adsorbed generates a critical surface cascade, which dictates the surface chemistry and biological properties of the nanoparticle. This outer polyelectrolyte layer dramatically affects not only the degree of nonspecific particle uptake, but also the nanoparticle biodistribution. For hyaluronic acid (HA) outer layers, a long blood elimination half-life (~9 h) and low accumulation (~ 10–15 % recovered fluorescence/g) in the liver were observed, illustrating that these systems can be designed to be highly appropriate for clinical translation.

Keywords

Layer-by-layer; Nanoparticles; Drug Delivery; Biomaterials

Introduction

The layer-by-layer (LbL) assembly of polyelectrolyte layers on solid surfaces is a well-established technique for generating functional thin films for applications in biosensing, drug and gene delivery, regenerative medicine, tissue engineering and biomimetics research[1, 2]. The popularity of this technique in the biomedical engineering community stems from the fact that many therapeutics and biologically relevant materials can be easily introduced into LbL films non-covalently and under physiological conditions, without significant alteration of their biological properties. In addition, because the films are formed a nano-layer at a time, it is possible to achieve nanometer scale precision over the composition and the internal structure of the resultant multi-component films[3, 4]. Together, these factors have facilitated the creation of specialized thin film structures with sophisticated levels of spatial, temporal or active control over the release of therapeutics from the surfaces of macroscopic objects.

Several years ago, the demonstration that conformal polyelectrolyte film coatings can be fabricated around gold nanoparticles via LbL presented exciting new opportunities for extending the use of this technology to nanoparticle delivery systems[5–7]. The versatility in manipulating the composition, surface chemistry and dimensions of nanostructured thin films on nanoscopic objects, when combined with the rich diversity of therapeutic moieties that are adaptable to this technique, provides a powerful tool for the nano-scale assembly of novel particle delivery systems. With LbL, there is also the capacity for incorporating a diverse range of biologics in predefined stoichiometric ratios with the ability to apply control over the release of each individual entrapped species from a single nanoscopic platform. This capability is especially beneficial to combinatorial therapeutic strategies aimed at inducing synergism among the delivered therapeutics. With appropriate use of blocking or barrier layers between film components, it is possible to achieve sequential release of drugs from LbL films, which implies the ability to not only tailor the types of therapeutics released, but also the order and timing in which they are released[8–10]. This capability could lead to powerful new approaches to delivery of synergistic therapies for cancer, infectious disease and other conditions.

As a result, a growing number of examples have demonstrated the utility of LbL based nano- and microparticle systems for a range of medical applications[11–15]. The majority of them highlight their use as platforms for controlled release of therapeutics after on-site administration, but a few recent studies have shown that these are also promising systems for applications that require systemic administration[16–19]. Furthermore, the concepts of alternating charge that are the basis of LbL assembly have also been of great interest for nucleic acid delivery. The formation of positively charged DNA/RNA polyplexes with polycations like polyethyleneimine (PEI) is one of the primary means of condensing and delivering nucleic acids; the addition of counterions to the polyplex structure showed improved transfection[20] *in vitro* and similar attempts have been made to limit PEI toxicity *in vivo* by generating negatively charged polyplexes using ‘recharging’ approaches[21]. Despite these recent demonstrations, the basic design principles governing the pharmacokinetics of this non-contemporary nanoparticle delivery system has not been addressed sufficiently to expand their use for systemic nanomedicine applications. Of particular interest are studies examining the influence of film architecture on *in vivo* stability, biodistribution, tissue interaction and other vital pharmacokinetic behavior, which are important prerequisite knowledge needed to allow the continued development of these systems.

To build knowledge in this area, model systems were created to demonstrate how changes in film architecture affect their *in vivo* pharmacokinetics. We identified key control parameters for improving *in vivo* LbL film stability and for controlling particle biodistribution. Focusing on cancer applications, we subsequently tuned the LbL films on nanoparticles to allow targeting of the system to solid tumors. Nanoparticle delivery of therapeutics to pathologic tissue is one of the most promising avenues for more efficacious and better-tolerated therapies[22, 23]; and these LbL systems have much to offer those that work toward the development of drug carriers. The work presented here represents a first look at how LbL nanoparticle films can be designed for their systemic delivery. In addition, it is also relevant to the greater biomedical engineering and biomaterials community, as it establishes a greater understanding of how electrostatically assembled systems function *in vivo* and how their biodistribution may be impacted not only by size and charge, but by the specific choice of polyion and its structure on the surface. This understanding is important for a range of nanomedicine applications, especially those based on LbL technology.

LbL Film Construction on Nanoparticles

The schematic for an LbL-based nanoparticle system capable of delivering multiple classes of therapeutics and releasing them in a programmable manner is shown in Fig. 1. The multi-component nanofilm built around a core template forms a crucial structural component of the LbL nanoparticle, and is responsible for transporting and controlling the release of therapeutics as well as imparting *in vivo* functionality. LbL nanoparticle cores can be made hollow to allow compartmentalization of biologics[24] or left as a solid template structure. Several material options are available for use as the solid core template, from metal or metal oxides to commercial degradable polymers, either to provide further multi-functionality or to compartmentalize another reservoir of drugs; but this aspect of LbL nanoparticle design will not be explored in this paper.

We built LbL nanofilms on two types of core templates (gold nanoparticles (AuNPs) and quantum dots (QD)), both with sizes of ~ 20 nm and carboxyl functional groups presented on their surfaces. The zeta potentials of both core nanoparticle templates are ~ −25 mV above pH 4.5. AuNPs serve as a convenient model system from which we can obtain precise information on their state of aggregation by measuring their plasmon shift[5, 25]. This feature makes the gold nanoparticle core a useful tool for determining optimal LbL assembly conditions (see Experimental Section), which are especially critical for the deposition of LbL films on nanoscopic objects due to the high potential for particle aggregation and loss of yield during assembly[26]. The plasmon shift can originate from two different phenomena: 1) the deposition of polyelectrolyte layers onto the particle surface, which typically results in a dielectric environment that shifts frequencies by less than 10 nm; and 2) the aggregation of multiple particles which causes a much more pronounced shift of more than 150 nm.

In order to bring these systems closer to biomedical translation, it is necessary to construct films composed entirely of biocompatible or biodegradable elements; we chose to use known biopolymers to create LbL nanoparticle systems. Using a dextran sulfate (DXS, 10 kDa) and poly-L-lysine (PLL, 10 kDa) polyelectrolyte pair, up to 10 polyelectrolyte layers were deposited on AuNPs. Based on zeta potential and light scattering analysis, an increase in the effective diameter and reversal of the zeta potential of the nanoparticles after each layering step confirmed the construction of LbL nanofilms around the AuNPs (Fig. 2a and 2b). The UV-vis spectra and peak shift for the particles are shown in Fig. S1 and Fig. 2C respectively. The plasmon bands have a peak that is increasing between ~ 525 nm to ~ 532 nm, corresponding to a red shift of about 1–2 nm per layer; this indicates polymer deposition on the nanoparticle with low levels of aggregation. The state of aggregation of AuNPs can also be followed visibly by a change in color of the solution from wine red to a purple-blue (Fig. 2D). The resultant color of the LbL particle colloidal solution (AuNP/$(PLL/DXS)_5$) maintained a wine red color, further evidence that the majority of the particles remain non aggregated under the chosen assembly conditions for up to 10 layers. The assembly of LbL films on AuNPs was attempted for a total of 20 layers, but significant aggregation of nanoparticles was observed during layers 15 – 20. In the future, more effective means of producing multi-layered LbL nanoparticles are necessary to expand the capabilities of these systems. The morphology of the particles was examined with AFM (Fig. 2E) and TEM (Fig. 2F). AFM images of the particles before and after 10 layers show a uniform increase in particle size, with the particles preserving their spherical shape after layering. TEM analysis of a single LbL particle shows the presence of a thin LbL shell constructed around a gold nanoparticle, confirming the creation of LbL nanofilms on AuNPs.

Stability of LbL-based Nanoparticle Systems *In Vivo*

The reticuloendothelial system and related components, circulating macrophages, renal and biliary clearance as well as the overall shear and dilution effects of blood represent the first important barrier posed to any systemically administered nanoparticle based therapy[27, 28]. Conventional nanoparticles capable of passively targeting solid tumors via the enhanced permeation and retention (EPR) effect[29] are typically designed to be structurally stable in blood, between 10 nm to 200 nm in size and with an anti-fouling surface that is hydrophilic and either neutral or slightly negative in charge. When combined, these features allow nanoparticles to circulate for longer periods of time so that the accumulated nanoparticles can reach therapeutic levels. To replicate these design features on LbL-based nanoparticles, an appropriate number of layers (PLL/DXS) are deposited to manipulate particle size, which are terminally capped with a layer of polyelectrolyte that is negatively charged and antifouling. For *in vivo* experimentation, this simple film architecture was built around carboxyl functionalized QD_{705}, which have similar sizes and zeta potentials to AuNPs. Unlike AuNPs, QD_{705} can be tracked *in vivo*, and this feature, together with the incorporation of a layer of PLL labeled with a near IR dye (PLL_{800}, ex/em: 785/800 nm), allows insight into the stability of the nanofilms as well as the LbL nanoparticle by real-time fluorescent tracking of their *in vivo* fate. The model systems described here are thus abbreviated as $QD_{705}/PLL_{800}/[DXS/PLL]_n$/[DXS or HA (hyaluronic acid)]. Both DXS and HA are negatively charged linear polysaccharides at physiological pH with reported anti-fouling properties, and are being investigated as biomimetic alternatives[30, 31] to poly(ethylene glycol)[32] as hydrated 'stealth' coatings that prevent protein adsorption and opsonization. The growth curves and zeta potentials of these particles are given in the Fig. S2. The doses given are similar and based on a calibration of QD_{705} fluorescence (see experimental section).

If the LbL films on our model systems are unstable *in vivo*, they fall apart and low molecular weight polymers like PLL_{800} (15 kDa) will be filtered from the blood by the kidneys[33], which can then be rapidly detected in the bladder (for example, see Fig. S3A); therefore, early detection of high concentrations of PLL_{800} in the bladder after injection of the LbL particles is an indication of their instability *in vivo*. We hypothesize that a gradual decomplexation process would eventually be responsible for the breakdown of these particles, which may lead to the accumulation of PLL_{800} in the bladder at much later time points. The results of an *in vivo* stability study are shown in Fig. 3. After single bilayer nanoparticles (n=0) terminated with either dextran sulfate (QD_{705}/PLL_{800}/DXS) or hyaluronic acid (QD_{705}/PLL_{800}/HA) were injected, a strong PLL_{800} bladder signal can be seen after ~ 30 min and ~4 h for QD_{705}/PLL_{800}/DXS and QD_{705}/PLL_{800}/HA particles respectively, indicating the destabilization of the layers over these time periods. Near-IR mouse images depicting these events are given in Fig. 3A(i) and Fig. S3. Although the single bilayer films eventually destabilized, there was a significant delay in time taken to observe bladder accumulation in contrast to injections of free PLL_{800}, signifying that some degree of stability is afforded by incorporating PLL_{800} into films. Additionally, the difference in times taken for QD_{705}/PLL_{800}/HA and QD_{705}/PLL_{800}/DXS particles to destabilize shows that the choice of the terminal polyelectrolyte layer is another factor that contributes to the stability of LbL films. When the number of bilayers was increased (n=3), a marked improvement in the stability of the nanofilms was observed in general. This can be clearly seen in Fig. 3A, where compared to the single bilayer films (Fig. 3A(i)), only a weak PLL_{800} bladder signal was detected from a portion of the mice injected with $QD_{705}/PLL_{800}/[DXS/PLL]_3$/DXS after 30 min and no bladder signal was found in mice injected with $QD_{705}/PLL_{800}/[DXS/PLL]_3$/HA. Changing the order of the PLL_{800} layer to a position adjacent to the HA terminal layer (Fig. 3A(iv)) yielded similar results, demonstrating the structural stability of the entire HA terminated tri-bilayer film. Overall, these findings show

that the number of layers, and to a degree, the terminal layer, are key variables in promoting LbL film stability. The observation that systemic stability of LbL films increases with the number of deposited layers is not surprising; electrostatically assembled LbL films are held together by ionic interactions between interpenetrated polymer layers. An increase in the number of deposited layers would increase the number of inter-layer ionic crosslinks, and would enhance the cohesion and mechanical stability of the film. This distinguishing trait of LbL systems therefore provides a convenient approach for tuning the stability of LbL assembled nano- and microparticles for applications *in vivo*. Similar observations have been made after assessment of LbL microcapsules in a subcutaneous environment[13]; and this study further demonstrates that tuning film stability with increased layer deposition is also a viable approach for generating stable particles in harsher systemic environments.

Biodistribution of Nanoparticles

Based on data obtained from real time intravital imaging, a key observation made was that the terminal layer of the LbL nanoparticles played a vital role in their biodistribution. Clear differences were found in the levels of liver accumulation between the two differently terminated LbL particles. Strong QD_{705} and PLL_{800} signals were always detected in the livers of all mice that received $QD_{705}/PLL_{800}/[DXS/PLL]_3/DXS$ but were weak in mice injected with $QD_{705}/PLL_{800}/[DXS/PLL]_3/HA$ (Fig. 3B). The images of mice showing colocalization of QD_{705} and PLL_{800} signals for both particles shown in Fig. 3B and Fig. S4, together with the lack of a PLL_{800} bladder signal during the experimental period (Fig. 3A(ii–iv)), confirm that these particles are truly stable and are retained by cells in the liver. To further examine the contribution of the terminal layer to particle trafficking *in vivo*, biodistribution studies were performed. The distribution of a single dose of injected LbL particles with different terminal layers as well as free QD_{705} and PLL_{800} at the 4 h time point after injection was determined with ex vivo fluorescence imaging of macerated tissue (3–5 mice per treatment) on both the QD_{705} and PLL_{800} channel; these fluorescence values were normalized by tissue weight and presented as the percentage injected per gram of tissue. From Fig. 3C and 3D, the similar biodistribution trends for both LbL nanoparticles determined on the two fluorescent channels reaffirm the stability of these systems. Both $QD_{705}/PLL_{800}/[DXS/PLL]_3/DXS$ and $QD_{705}/PLL_{800}/[DXS/PLL]_3/HA$ particles were mainly found in the liver (~ 35–45 %rf/g and ~ 10–15 %rf/g respectively) and spleen (~ 15–20 %rf/g and ~ 15 %rf/g respectively); the weak signals detected in the kidneys, heart and lungs are attributed to nanoparticles in blood that remained in these organs after their extraction. The increased liver accumulation of $QD_{705}/PLL_{800}/[DXS/PLL]_3/DXS$ particles over $QD_{705}/PLL_{800}/[DXS/PLL]_3/HA$ particles is consistent with our observations using near IR intravital imaging. As expected, the biodistribution of free QD_{705}, PLL_{800} and PLL terminated $QD_{705}/PLL_{800}/[DXS/PLL]_4$ were markedly different from the negatively charged HA and DXS terminated LbL nanoparticles. Importantly, significant levels of PLL_{800} and $QD_{705}/PLL_{800}/[DXS/PLL]_4$ were detected in the kidneys and lungs; and in general, higher biodistribution levels were noted in both the liver and spleen. As any circulating low molecular weight polymer is expected to be cleared rapidly by renal filtration, the retention of positively charged PLL_{800} in the kidneys and lungs is likely due to its non-specific interactions with cells in these highly vascularized organs. Positively charged $QD_{705}/PLL_{800}/[DXS/PLL]_4$ particles, which have a layer of exposed PLL on the surface also interact directly with cells in the same manner as PLL_{800}, causing their uptake and accumulation in these organs. Positively charged species in vivo also readily adsorb to opsonins, leading to pronounced RES uptake in the liver and spleen[34, 35]. A single terminal layer of antifouling polysaccharide prevented cellular and protein interaction with the nanoparticles, and the biodistribution pattern changes to favor only the liver and spleen. The presence of this terminal layer actively reduces RES involvement, as evidenced by the significantly higher levels of free QD_{705}, in the liver and spleen. Representative fluorescent

images of whole tissue showing the distribution of QD_{705} and PLL_{800} are provided in Fig. S5 to help understand the different biodistribution patterns more visually.

We have achieved, via optimizing the architecture of LbL nanofilms, stable nanoparticles with biodistribution profiles comparable to the most promising block copolymer delivery systems[36–38]; and this is particularly evident in their low degrees of uptake (~ 10–15 %rf/g) by the liver and spleen, which are among the lowest numbers observed for any nanoparticle delivery system. Due to the presence of scavenging cells, the liver typically accounts for a significant portion of the biodistribution of systemically administered nanoparticles[39]. For applications that aim to target tumors, the undesirable level of nanoparticle accumulation in the liver and spleen, which can be as high as ~ 40 %rf/g[39, 40], can result in reduced delivery to tumors. Further modulation of liver accumulation of LbL particles, achieved via the selection of the appropriate terminal layer, would likely improve EPR-based targeting to solid tumors as well as reduce the potential toxicity to the liver and other important organs. Knowledge gained from this study would not only facilitate future development of LbL particle systems, but should also be relevant to other electrostatically assembled nucleic acid delivery systems[20, 21], which are formed from complexing nucleic acids and polyelectrolytes that mediate transfection (PEI). As the underlying mechanisms influencing complex formation and transfection efficacy are similar to LbL, the same rules may apply toward improved stability and biodistribution of the complexes *in vivo*.

Passive Tumor Targeting of Long Circulating LbL Nanoparticles

To assess the use of optimized LbL nanoparticles for cancer delivery, we tested their ability to target solid tumors via EPR. The stability and biodistribution profile of multi-layered, HA terminated films *in vivo* indicate that they might be able to extend the circulation times of LbL nanoparticles to levels sufficient for passive targeting to solid tumors via EPR. Three particles were tested for their blood circulation profile: 1) free QD_{705}, 2) QD_{705}/PLL/[DXS/PLL]$_3$/DXS particles and 3) (QD_{705}/PLL/[DXS/PLL]$_3$/HA) particles. After systemic intravenous injection in mice (via tail vein), the blood concentrations of the nanoparticles decreased in a two-phase manner (Fig. 4A). All particles were observed to undergo a rapid distribution phase within 1 h of injection. After 10 h, QD_{705} were no longer detected in the blood, while blood concentrations of QD_{705}/PLL/[DXS/PLL]$_3$/DXS and QD_{705}/PLL/[DXS/PLL]$_3$/HA particles dropped to ~ 7% and ~29% respectively. Using a two compartment model[41], we estimate that the distribution and elimination half-lives for QD_{705}/PLL/[DXS/PLL]$_3$/DXS particles are 0.16 h and 3.2 h respectively, while the half-lives for QD_{705}/PLL/[DXS/PLL]$_3$/HA particles are 0.21 h and 8.4 h respectively. The longer persistence of QD_{705}/PLL/[DXS/PLL]$_3$/HA in the blood stream corroborates their superior stability and biodistribution profile. The whole body fluorescence intensity of mice given QD_{705}/PLL/[DXS/PLL]$_3$/HA particles (Fig. 3A) were also observed to be higher when compared to other systems for up to 24 h. We next monitored the accumulation of the QD_{705}/PLL/[DXS/PLL]$_3$/HA particles in subcutaneously induced KB tumors with intravital fluorescence imaging over a period of 72 h. At 24 h post injection, QD_{705}/PLL/[DXS/PLL]$_3$/HA particles were detectable in tumors (Fig. 4B) and the time dependent nanoparticle signal from the tumors is given in Fig. 4C. KB tumors are not know to express significant levels of CD44[42], the receptor for hyaluronic acid and therefore, the nanoparticle accumulation and clearance profile in the tumor is typical of EPR based targeting, which is short-lived as there are no active mechanisms in place to promote cell uptake or extend their residence time in the tumor interstitials.

Examining Reasons for the Different Biodistribution of HA and DXS Terminated LbL Nanoparticles

In an attempt to understand the different liver retention of HA and DXS terminated particles, we examined the involvement of liver receptors in taking up the differently coated LbL nanoparticles, as well as the degree of particle phagocytosis by macrophages to account for RES involvement. The liver sinusoidal endothelial cells (LSEC) present a variety of different receptors that scavenge blood for soluble macromolecules[43]. Biological polysaccharides like HA bind to some of these receptors, but this can be inhibited by sulfated polysaccharides like DXS and chondroitin sulfate (CS), which show greater specificity to these liver receptors[44, 45]. Our observations that DXS terminated LbL nanoparticles accumulate in the liver more significantly than those that are HA terminated suggest that this receptor-mediated mechanism is also relevant when HA or DXS is used as the terminal layer on LbL nanoparticles. To investigate this, QD_{705}/PLL/$[DXS/PLL]_3$/DXS particle injections were competed with co-injections of free (~10 kDa) DXS and HA (10 mg/kg each). Fig. 5A shows the degree of liver accumulation of QD_{705}/PLL_{800}/$[DXS/PLL]_3$/DXS with and without free DXS or HA competition in the liver 4 h after injection. An image of a representative mouse for each treatment taken in a single viewing field is shown in Fig. S6 and plots of the time dependent accumulation of particles in the liver are given in Fig. S7. When free dextran sulfate was co-injected with QD_{705}/PLL/$[DXS/PLL]_3$/DXS, the levels of its liver accumulation were significantly lower. This effect was not observed with co-injections of HA at the same dose. These observations suggest that the stronger liver accumulation of dextran sulfate terminated LbL particles could be due to uptake mechanisms in the liver that are specific to dextran sulfate. In addition to their different surface chemistry, recent studies also suggest that the stronger negative surface charge of DXS terminated systems could have contributed to their higher liver accumulation[35].

Phagocytosis of both opsonized and non-opsonized LbL nanoparticles was examined *in vitro* using mouse macrophages to give insight into the role that the RES (kupffer cells) plays in influencing LbL nanoparticle accumulation in the liver. We found that these processes did not exhibit a strong dependence on HA or DXS terminated nanoparticles (Fig. 5B). Compared to free QD_{705}, LbL nanoparticles terminated with either HA or DXS bound to IgG, a major class of opsonins, to a lesser extent than free QD_{705}, owing to the formation of an antifouling layer around the nanoparticle (Fig. S8A, S8B and S8C); this subsequently led to lower levels of phagocytosis when compared to opsonized QD_{705}. As no significant differences were found for both the opsonization and the phagocytosis of HA and DXS terminated LbL nanoparticles, RES uptake does not appear to play an important role in the different liver accumulations for these two negatively charged exterior layered systems. The biodistribution data in Fig. 3C and 3D support this conclusion, as only liver uptake of the LbL nanoparticles were notably different, even though splenic cells are known to constitute part of the RES system. Finally, an *in vitro* examination of the aggregation behavior of these particles was also performed to help account for their biodistribution. Although DXS terminated particles exhibited a slight degree of aggregation over a 12 h period (Fig. S8D), we do not expect this behavior to have affected its biodistribution *in vivo*, in light of our observation that free DXS competes with DXS terminated nanoparticles in the liver and the lack of their accumulation in the lungs (Fig. 3C and 3D), where the capillary beds are a typical accumulation point for large aggregates. Looking forward, work examining the influence of the terminal polyelectrolyte layer on tissue or cell receptor interactions is crucial to these systems and is on going in our laboratory.

Conclusion

We have elucidated the critical nature of the LbL film composition and its effects on the pharmacokinetics of LbL-based nanoparticle systems. Optimizing the LbL films enabled the generation of stable nanoparticles for systemic cancer applications. Our findings highlight unique aspects of this alternative nanoparticle system: the electrostatically assembled nanoparticles gain increased stability *in vivo* with increased numbers of adsorbed film layers, and the final layer deposited is an important surface layer, which dictates the surface and biological properties of the nanoparticle, and is therefore an important variable to control to affect the biodistribution of the LbL nanoparticle. Finally, the potential for LbL-based nanoparticles to entrap a diverse range of therapeutics and allow further control over dosage and regimen from a single nanoscopic platform opens new avenues for drug delivery. To unlock this capability, future work examining the loading and programmed release of biologics in concert with LbL nanoparticle pharmacokinetics and cell uptake is necessary.

Materials and Methods

For a full description, please refer to the Supporting Information.

Materials

All chemicals and biological material were purchased from Sigma-Aldrich or Invitrogen unless otherwise noted.

In vivo experimentation

BALB/c mice were used for blood circulation experiments and the NCr nudes were used for all other experiments. Mice fed on AIN-76A diet for at least a week were given single injections of the different LbL particles via the tail vein. The concentration of particles (QD_{705} and LbL nanoparticles) administered was ~ 0.5 μM given in 0.1 mL injection. Free PLL_{800} was administered at doses of 5 mg/kg. At various time points after injection, they were imaged ventrally using the IVIS system (Caliper Lifescience). Living Image software Version 3.0 (Xenogen) was used to acquire and quantitate the fluorescence. The images showing QD_{705} fluorescence was captured using Ex: 640 nm and Em: 720 nm. The images showing PLL_{800} fluorescence was captured using Ex: 710 nm and Em: 800 nm. Spectrally unmixed images were captured using a sequence of Ex: 640 nm and Em: 700 nm/720 nm/740 nm/760 nm for QD_{705}; and Ex: 745 nm and Em: 800 nm/820 nm/840 nm for PLL_{800}. Subcutaneous tumors were induced in either the left or right hind flank of NCr nudes after injection of ~1–2 million cells (KB) in 0.1 mL media. Tumors were allowed to grow to ~100 mm^3 before experimentation. Where applicable, tissue samples were extracted for further imaging using the Licor Odyssey system. For biodistribution, tissue samples were harvested, washed, weighed, and macerated in well plates and imaged with the IVIS system for their respective fluorescence. The percent-recovered fluorescence was normalized by tissue weight. Blood circulation analysis was performed by measuring the remaining QD signal from blood taken after injection with the Licor Odyssey system.

Supplementary Material

Refer to Web version on PubMed Central for supplementary material.

Acknowledgments

We wish to thank our funding source for this research, the National Institutes of Health (NIH) NIBIB grant R01EB008082. We also thank the Koch Institute (MIT), the Institute for Soldier Nanotechnology (ISN) and the department of comparative medicine (DCM) at MIT for assistance with animal experiments and for use of facilities.

References

1. Decher G, Eckle M, Schmitt J, Struth B. Current Opinion in Colloid & Interface Science. 1998; 3(1):32–39.
2. Boudou T, Crouzier T, Ren K, Blin G, Picart C. Advanced Materials (Weinheim, Germany). 2010; 22(4):441–467.
3. Hammond PT. Advanced Materials (Weinheim, Germany). 2004; 16(15):1271–1293.
4. Lynn DM. Advanced Materials (Weinheim, Germany). 2007; 19(23):4118–4130.
5. Gittins DI, Caruso F. J. Phys. Chem. B. 2001; 105(29):6846–6852.
6. Gittins DI, Caruso F. Advanced Materials (Weinheim, Germany). 2000; 12(24):1947–1949.
7. Mayya KS, Schoeler B, Caruso F. Advanced Functional Materials. 2003; 13(3):183–188.
8. Wood K, Zacharia NS, Schimidt DJ, Wrightman SN, Andaya BJ, Hammond PT. Proc. Natl. Acad. Sci. U. S. A. 2008; 105(7):2280–2285. [PubMed: 18272499]
9. Liu X, Zhang J, Lynn DM. Advanced Materials (Weinheim, Germany). 2008; 20(21):4148–4153.
10. Zhang J, Lynn DM. Advanced Materials (Weinheim, Germany). 2007; 19(23):4218–4223.
11. Becker AL, Johnston APR, Caruso F. Small. 2010; 6(17):1836–1852. [PubMed: 20715072]
12. Facca S, Cortez C, Mendoza-Palomares C, Messadeq N, Dierich A, Johnston APR, Mainard D, Voegel JC, Caruso F, Benkirane-Jessel N. Proc. Natl. Acad. Sci. U. S. A. 2010; 107(8):3406–3411. S3406/1-S3406/4. [PubMed: 20160118]
13. De KS, De GBG, Cuvelier C, Ferdinande L, Deckers W, Hennink WE, De SS, Mertens N. Advanced Functional Materials. 2007; 17(18):3754–3763.
14. Yan Y, Johnston APR, Dodds SJ, Kamphuis MMJ, Ferguson C, Parton RG, Nice EC, Heath JK, Caruso F. ACS Nano. 2010; 4(5):2928–2936. [PubMed: 20420377]
15. Akita H, Kudo A, Minoura A, Yamaguti M, Khalil IA, Moriguchi R, Masuda T, Danev R, Nagayama K, Kogure K, Harashima H. Biomaterials. 2009; 30(15):2940–2949. [PubMed: 19261326]
16. Sexton A, Whitney PG, Chong S-F, Zelikin AN, Johnston APR, De RR, Brooks AG, Caruso F, Kent SJ. ACS Nano. 2009; 3(11):3391–3400. [PubMed: 19824668]
17. Zhao Q, Han B, Wang Z, Gao C, Peng C, Shen J. Nanomedicine (N. Y., NY, U. S.). 2007; 3(1): 63–74.
18. Elbakry A, Zaky A, Liebl R, Rachel R, Goepferich A, Breunig M. Nano Letters. 2009; 9(5):2059–2064. [PubMed: 19331425]
19. Schneider GF, Subr V, Ulbrich K, Decher G. Nano Letters. 2009; 9(2):636–642. [PubMed: 19170551]
20. Saul JM, Wang C-HK, Ng CP, Pun SH. Advanced Materials (Weinheim, Germany). 2008; 20(1): 19–25.
21. Trubetskoy VS, Wong SC, Subbotin V, Budker VG, Loomis A, Hagstrom JE, Wolff JA. Gene Ther. 2003; 10(3):261–271. [PubMed: 12571634]
22. Allen TM, Cullis PR. Science (Washington, DC, U. S.). 2004; 303(5665):1818–1822.
23. Duncan R. Nature Reviews Cancer. 2006; 6(9):688–701.
24. Angelatos AS, Katagiri K, Caruso F. Soft Matter. 2006; 2(1):18–23.
25. Schneider GF, Decher G. Nano Letters. 2008; 8(11):3598–3604. [PubMed: 18850753]
26. Schneider G, Decher G. Langmuir. 2008; 24(5):1778–1789. [PubMed: 18225923]
27. Haag R, Kratz F. Angew. Chem., Int. Ed. 2006; 45(8):1198–1215.
28. Petros RA, De SJM. Nat. Rev. Drug Discovery. 2010; 9(8):615–627.
29. Maeda H, Wu J, Sawa T, Matsumura Y, Hori K. J. Controlled Release. 2000; 65(1–2):271–284.

30. Perrino C, Lee S, Choi SW, Maruyama A, Spencer ND. Langmuir. 2008; 24(16):8850–8856. [PubMed: 18616303]
31. Lee Y, Lee H, Kim YB, Kim J, Hyeon T, Park H, Messersmith PB, Park TG. Advanced Materials (Weinheim, Germany). 2008; 20(21):4154–4157.
32. Duncan R. Nat. Rev. Drug Discovery. 2003; 2(5):347–360.
33. Fox ME, Szoka FC, Frechet JMJ. Acc. Chem. Res. 2009; 42(8):1141–1151. [PubMed: 19555070]
34. Balogh L, Nigavekar SS, Nair BM, Lesniak W, Zhang C, Sung LY, Kariapper MST, El-Jawahri A, Llanes M, Bolton B, Mamou F, Tan W, Hutson A, Minc L, Khan MK. Nanomedicine (N. Y., NY, U. S.). 2007; 3(4):281–296.
35. Xiao K, Li Y, Luo J, Lee JS, Xiao W, Gonik AM, Agarwal RG, Lam KS. Biomaterials. 2011; 32(13):3435–3446. [PubMed: 21295849]
36. Cheng J, Teply BA, Sherifi I, Sung J, Luther G, Gu FX, Levy-Nissenbaum E, Radovic-Moreno AF, Langer R, Farokhzad OC. Biomaterials. 2006; 28(5):869–876. [PubMed: 17055572]
37. Kwon GS, Yokoyama M, Okano T, Sakurai Y, Kataoka K. Pharm. Res. 1993; 10(7):970–974. [PubMed: 8378259]
38. Gratton SEA, Pohlhaus PD, Lee J, Guo J, Cho MJ, DeSimone JM. J. Controlled Release. 2007; 121(1–2):10–18.
39. Moghimi SM, Hunter AC, Murray JC. Pharmacological Reviews. 2001; 53(2):283–318. [PubMed: 11356986]
40. Semete B, Booysen L, Lemmer Y, Kalombo L, Katata L, Verschoor J, Swai HS. Nanomedicine (Philadelphia, PA, U. S.). 2010; 6(5):662–671.
41. Rowland M, Benet LZ, Graham GG. J Pharmacokinet Biopharm. 1973; 1(2):123–136. [PubMed: 4764426]
42. Segawa E, Kishimoto H, Takaoka K, Noguchi K, Hashitani S, Sakurai K, Urade M. Oncol. Rep. 24(3):733–739. [PubMed: 20664981]
43. Smedsrod B, De BPJ, Braet F, Lovisetti P, Vanderkerken K, Wisse E, Geerts A. Gut. 1994; 35(11): 1509–1516. [PubMed: 7828963]
44. Gustafson S, Bjorkman T. Glycoconj J. 1997; 14(5):561–568. [PubMed: 9298688]
45. Gustafson S. Glycobiology. 1997; 7(8):1209–1214. [PubMed: 9455922]

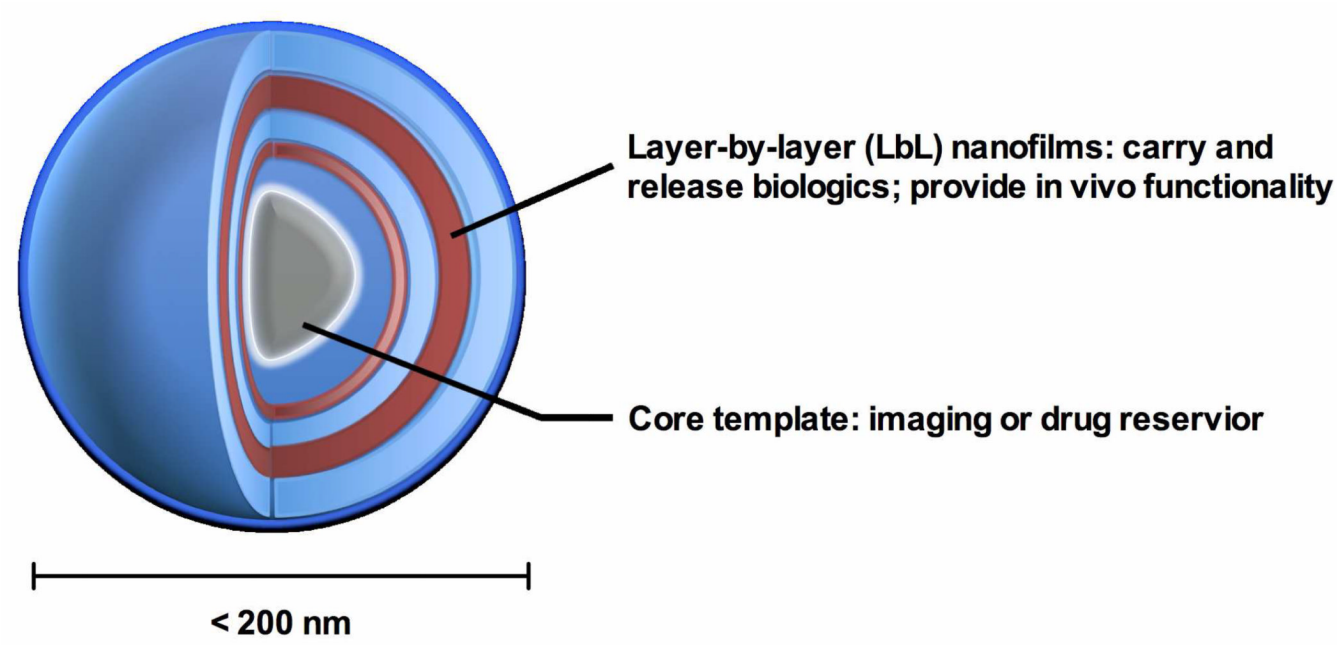

Fig. 1.

Schematic of a layer-by-layer (LbL) based nanoparticle delivery system. The stepwise assembly of nanofilms on a core nanscopic template allows nanometer scale precision over the compositions and the internal structures of the resultant multi-component, multi-functional films with sophisticated levels of temporal or active control over the presentation of biologics to cells from a single nanoparticle platform.

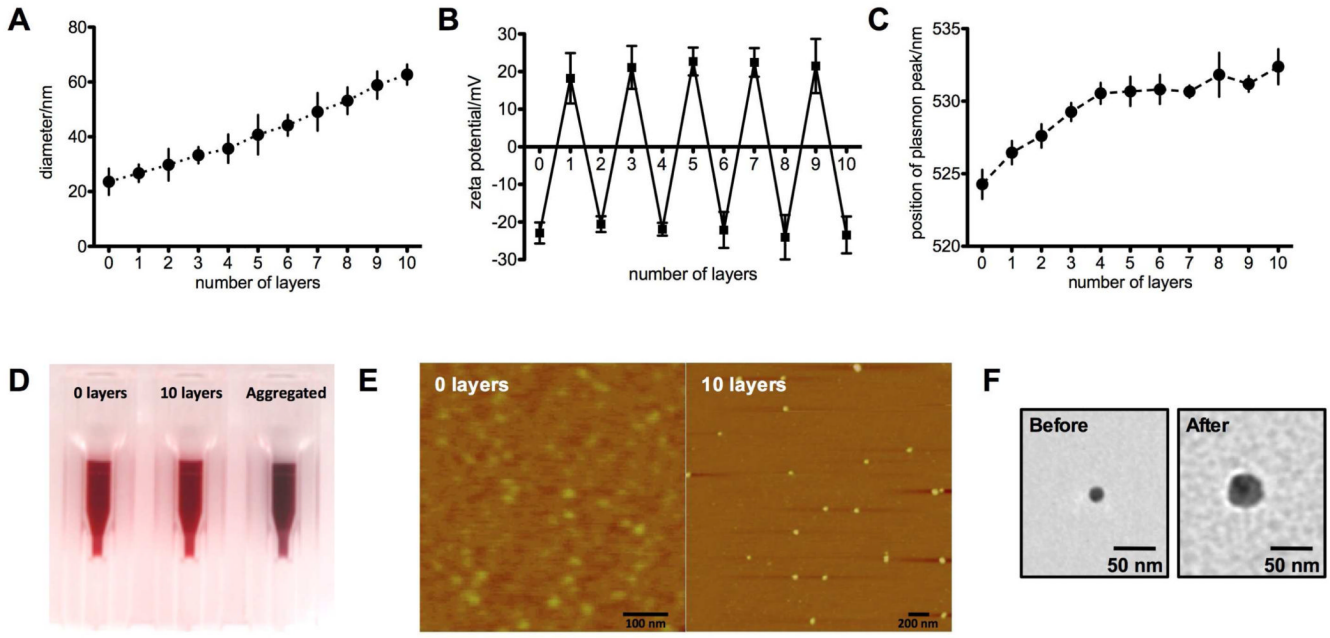

Fig. 2.

Characterization of LbL nanoparticles. A) The growth curve of PLL/DXS (poly-L-lysine/dextran sulfate) nanofilms deposited on AuNPs (gold nanoparticles) particles. Each layer is ~ 2 nm thick. B) The zeta potential of LbL particle after deposition of each PLL or DXS layer show complete reversal of charge. C) Position of plasmon peak of AuNPs after each step of the LbL deposition process. A small red shift of 1–2 nm per layer corresponds to the deposition of a nanofilm and not the aggregation of AuNPs. D) Photograph showing the color of dispersions of AuNPs before and after 10 layers of LbL film deposition confirming the non-aggregated state of AuNPs even after 10 layers of polyelectrolyte deposition. Assembly conditions are described in the experimental section. E) AFM images of LbL AuNPs before and after deposition of 10 polyelectrolyte layers. The resultant particles preserved a spherical shape and are uniform in size. F) Before and after TEM images showing a LbL coating of 4 bilayers around a AuNP core (AuNP/$(PLL/DXS)_4$). All data in Fig. 2 is given in mean±SEM, n = 5–10.

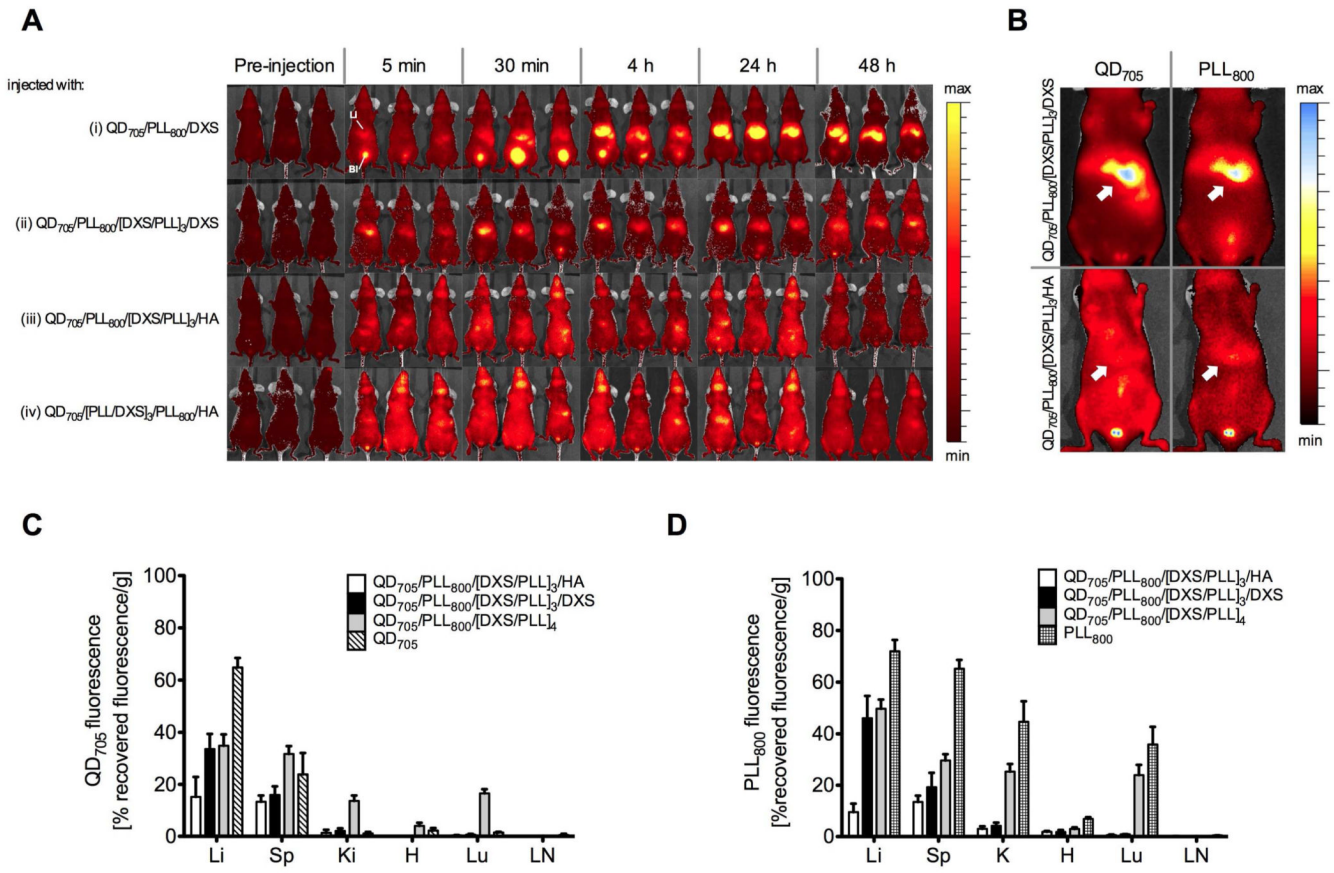

Fig. 3.

Systematic examination of the pharmacokinetics and biodistribution profile of LbL nanoparticles with different film architectures. A carboxyl functionalized quantum dot (QD_{705}) template was used to build the LbL nanoparticles to allow tracking of both the film (using PLL_{800}, a near-IR labeled poly-L-lysine layer (15 kDa, ex: 800nm)) and core (using QD_{705}, ex: 705 nm), which would allow more information on these systems to be obtained *in vivo*. Fig. S3 gives the close up images showing the anatomical positions of the liver and bladder of a mice from a ventral position to help with the analysis of these sets of data. A) The *in vivo* fate of LbL nanofilms with different architectures: (i) $QD_{705}/PLL_{800}/DXS$, (ii) $QD_{705}/PLL_{800}/[DXS/PLL]_3/DXS$, (iii) $QD_{705}/PLL_{800}/[DXS/PLL]_3/HA$, and (iv) $QD_{705}/[PLL/DXS]_3/PLL_{800}/HA$ are examined by tracking PLL_{800}. Only images from the 800 nm channels are shown. Single bilayer architectures (i) are unstable and the disassembled PLL_{800} localizes in the bladder and liver within 30 min. Multi-layered films grant more stability (ii, iii, iv); for these film architectures, the bladder PLL_{800} signal was either weakly or not detected. Stable DXS terminated LbL nanoparticles (ii) also preferentially accumulated in the liver and the liver PLL_{800} signal is due to the accumulation of the whole LbL nanoparticle, which is confirmed in Fig. 3B and Fig. S4. B) The arrows in the images show the co-localization of both nanoparticle film (PLL_{800}) and core (QD_{705}) in the livers of mice for the stable multi-layered LbL nanoparticles. c and d) Biodistribution of $QD_{705}/PLL_{800}/[DXS/PLL]_3/DXS$, $QD_{705}/PLL_{800}/[DXS/PLL]_3/HA$ and $QD_{705}/PLL_{800}/[DXS/PLL]_4$ particles, with QD_{705} and PLL_{800} controls monitored on the 700 nm (C) and 800 nm (D) channels. Data shown is normalized by tissue weight and presented as the percentage recovered fluorescence per gram of tissue (%rf/g) and given in mean±SEM (n = 3–5). The results show that a single terminal layer of antifouling polysaccharide is sufficient for

preventing cellular interaction with the PLL layer to shift the biodistribution pattern in favor of only the liver and spleen. Li=Liver, Sp=spleen, Ki=kidneys, H=heart, Lu=lungs and LN=lymph node.

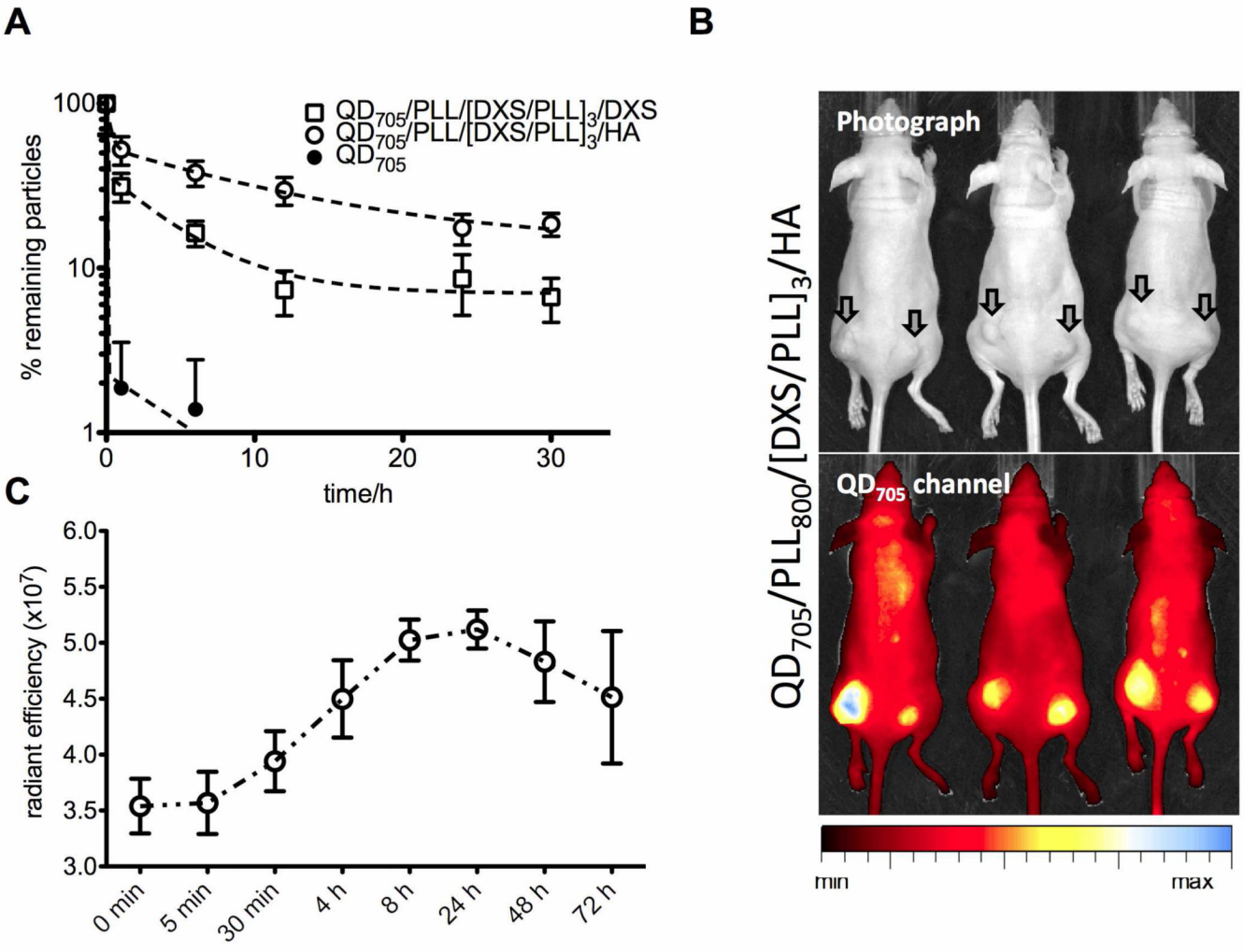

Fig. 4.

Blood circulation and tumor targeting of optimized LbL nanoparticles. A) Blood circulation profiles of QD_{705}, QD_{705}/PLL/$[DXS/PLL]_3$/HA and QD_{705}/PLL/$[DXS/PLL]_3$/DXS. The longer persistence of QD_{705}/PLL/$[DXS/PLL]_3$/HA in the blood stream corroborates their superior stability and biodistribution profile. B) Enhanced permeation and retention (EPR) based targeting of solid KB tumors induced subcutaneously on both hind flanks using QD_{705}/PLL/$[DXS/PLL]_3$/HA. Image is taken at the 24 h time point. C) Time dependant accumulation of QD_{705}/PLL/$[DXS/PLL]_3$/HA in KB tumors. Accumulation of the nanoparticles in tumors is transient and typical of EPR dominated targeting. Data is given in mean±SEM, n = 6.

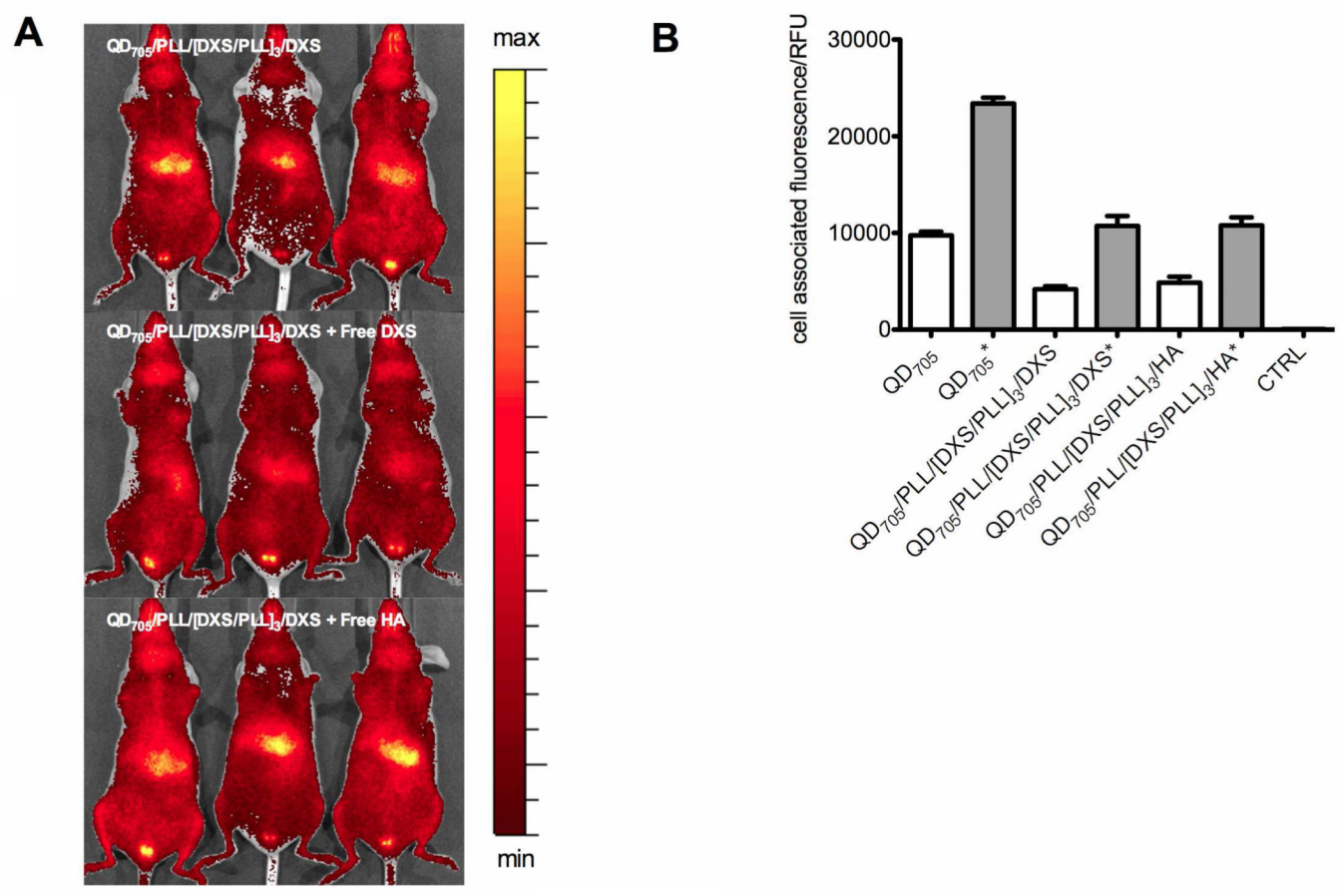

Fig. 5.

The effect of the terminal layer on LbL nanoparticle biodistribution. A) Images of mice receiving QD_{705}/PLL/[DXS/PLL]$_3$/DXS with co-injections of free DXS and HA (10 mg/kg) taken at the 4 h time point. Accumulation of QD_{705}/PLL_{800}/[DXS/PLL]$_3$/DXS particles in the liver is reduced with free DXS competition, suggesting a receptor mediated mechanism for the uptake of DXS terminated particles by the liver. B) Phagocytosis of nanoparticles determined by flow cytometry analysis of mouse macrophage J774A.1 cells after incubation with different nanoparticles. Opsonized nanoparticles are indicated with (*). Opsonized LbL nanoparticles terminated with HA or DXS show reduced uptake compared to opsonized QD_{705} but phagocytosis of both opsonized and non-opsonized LbL nanoparticles did not exhibit a strong dependence on their terminal layer. Data is given in mean±SEM for n = 5 with > 5000 events each. Representative raw flow cytometry histograms and confocal images showing phagocytosis are given in Fig. 7B and 7C.

Table 1

The sizes, zeta potentials and PDI the main LbL nanoparticles used for *in vivo* experimentation. Data is given in mean±SEM, n = 10.

	Effective Diameter (nm)	Zeta Potential (mV)	PDI
QD_{705}	~ 18 ± 5.2	~ −25 ± 3.6	1.13
$QD_{705}/PLL_{800}/[DXS/PLL]_3/DXS$	~ 47 ± 6.1	~ −30 ± 5.8	1.21
$QD_{705}/PLL_{800}/[DXS/PLL]_3/HA$	~ 50 ± 7.9	~ −20 ± 6.2	1.27
$QD_{705}/PLL_{800}/[DXS/PLL]_4$	~ 48 ± 6.6	~ +20 ± 4.5	1.22